Supplemental Material for:

Relaxation dynamics in the merging of N independent condensates

M. Aidelsburger, J. L. Ville, R. Saint-Jalm, S. Nascimbène, J. Dalibard, J. Beugnon

Laboratoire Kastler Brossel, Collège de France, CNRS, ENS-PSL Research University, UPMC-Sorbonne Universités, 11 place Marcelin-Berthelot, 75005 Paris, France

EXPERIMENTAL SEQUENCE

The experimental sequence started by loading a cold cloud ($> 500\,\text{nK}$) of ^{87}Rb atoms into a blue-detuned optical potential at wavelength $\lambda = 532\,\text{nm}$. In the vertical direction the atoms were confined by an optical accordion with an initial lattice spacing of $11\,\mu\text{m}$. The in-plane confinement was provided by an additional laser beam that was shaped with a digital micromirror device (DMD) to engineer almost arbitrary in-plane trapping geometries. A detailed description of the experimental setup can be found in Ref. [S1].

In order to optimize the final atom number in the double-ring trap, displayed in Fig. 1(b) of the main text, we loaded the atoms into a disk-shaped trap with a radius of about $30\,\mu\text{m}$. Using the dynamical mode of our DMD we then displayed a movie that successively changed the trap from the disk to the final double-ring configuration. The movie consisted of 20 images and had a duration of $0.2\,\text{s}$. The last image of this movie abruptly introduced the potential barriers to partition the outer ring into N individual segments. At the same time we compressed the optical accordion to a final lattice spacing of $5.6\,\mu\text{m}$ [S1]. This has the advantage that we can lower the power of the accordion beams, which reduces the strength of defects in the optical potential, while keeping a strong harmonic confinement along the z-direction.

As a next step we implemented a protocol to generate a reliable uniform phase in the inner ring, which is important for our interference-based detection technique [S2, S3]. In order to achieve that, we introduced an additional barrier in the inner ring simultaneously with the ones in the outer ring. This prevents the formation of random supercurrents in the inner ring during evaporation [S4]. We cooled the atoms within $2\,\text{s}$ by lowering the power of the dipole trap. Using an independent temperature calibration we extracted a final temperature of $T < 20\,\text{nK}$. This value corresponds to the lowest detectable temperature using our calibration method.

Subsequently, we slowly removed the barrier of the inner ring by displaying a movie of 19 images with our DMD that decreased the width of the barrier gradually in $1.9\,\text{s}$ from $2.5(2)\,\mu\text{m}$ to zero. This procedure ensures that we have a probability for creating a supercurrent in the inner ring that is $\lesssim 0.6\%$. This value was evaluated from an independent calibration measurement explained in the following section. Subsequently we merged the segments in the outer ring within $10\,\text{ms}$ by displaying a movie that consisted of 20 images on the DMD with decreasing barrier widths. We then let the system evolve for $500\,\text{ms}$ and performed a 2D time-of-flight (TOF). For that we suddenly switched off the in-plane trap while keeping a slightly increased vertical confinement with frequency $\omega_z = 2\pi \times 2\,\text{kHz}$. After an expansion time of $6\,\text{ms}$ we recorded the interference pattern along the z-direction using standard absorption imaging.

All in-situ images presented in this Letter were taken with partial imaging. The displayed densities correspond to 15% of the total density and the imaging intensity was about $I/I_\text{sat} = 0.2$, where $I_\text{sat} = 1.67\,\text{mW/cm}^2$. To obtain a better contrast for the time-of-flight images we imaged the total atomic density at higher imaging intensity $I/I_\text{sat} = 0.6$.
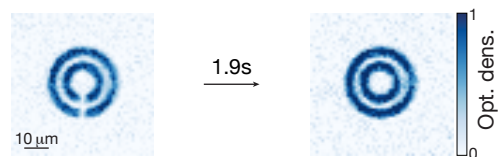

FIG. S1: Calibration measurement for the inner ring depicted in Fig. 1(b) of the main text which serves as a uniform phase reference in our detection scheme. In-situ images of the atoms in the double-ring trap averaged over 6 and 10 individual images respectively. Initially there is a $2.5(2)\,\mu\text{m}$-wide barrier in each ring (image on the left). The image on the right shows the atomic density distribution after removing the barriers in $1.9\,\text{s}$.

PHASE REFERENCE OF THE INNER RING

To investigate the formation of supercurrents in the inner ring using the protocol described in the previous section, we loaded the atoms into a double-ring trap with slightly smaller dimensions (Fig. S1). The outer ring has the same dimensions as the inner ring depicted in Fig. 1(b) of the main text, with an inner radius of $11\,\mu\text{m}$ and an outer one of $15\,\mu\text{m}$. The second ring is smaller with an inner radius of $5\,\mu\text{m}$ and an outer one of $9\,\mu\text{m}$. The experimental sequence started by loading the atoms into this double ring potential, where we have in-

troduced a 2.5(2) μm-wide barrier in both rings (Fig. S1). Using the detection method described above, we took $\mathcal{M} = 159$ measurements without observing any non-zero phase winding. In order to estimate the probability for non-zero phase windings in the ring we compute an upper bound according to the maximum likelihood estimation. According to this, the true probability $p(\nu \neq 1)$ is likely to be smaller than $1/159 = 0.6\%$ [S5].
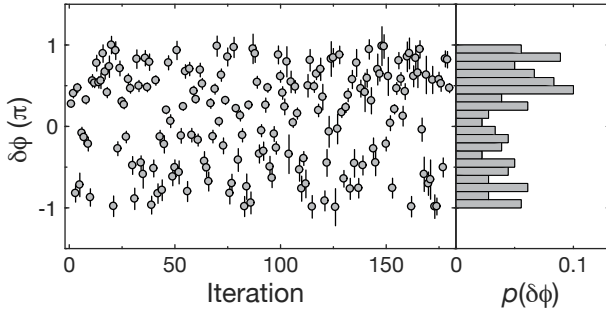

FIG. S2: Relative phase between the two ring-shaped condensates. The relative phases $\delta\phi$ were evaluated using the data displayed in Fig. 2(a) of the main text for $N = 1$ and restricting the analysis to images with $\nu = 0$. The results are shown in the left panel. The corresponding histogram displaying the binned probabilities $p(\delta\phi)$ is depicted in the right panel.

PREPARATION OF INDEPENDENT BECS

A crucial ingredient of our experimental protocol is the ability to form uncorrelated condensates in our trap via the introduction of additional potential barriers. The height of the potential is determined by the total depth of the optical potential and the width of $2.5(2)\,\mu$m is the full width at half maximum of the density dip in the in-situ distribution. In order to test the independence of the individual condensates we evaluated the relative phase $\delta\phi$ between two ring-shaped condensates with uniform phases separated by $2.5(2)\,\mu$m. For the analysis we took the data displayed in Fig. 2(a) for $N = 1$ and removed all images with non-zero phase winding. For each image we computed the radial average and subtracted the background obtained by the total average of all images. The resulting density modulation was fitted with a sinusoidal function $f(r) = A\sin(kr + \delta\phi)$ to determine the phase of the interference pattern $\delta\phi$ (Fig. S2). The period k was set to the mean period obtained from the individual fit results and the amplitude A and the phase offset $\delta\phi$ were free fit parameters. In total we have evaluated $\mathcal{M} = 180$ images, where we have excluded those, where the fit error of $\delta\phi$ exceeded 0.25π. The obtained distribution (Fig. S2) is characterized by the mean values: $\langle\cos(\delta\varphi)\rangle = 0.11(5)$ and $\langle\sin(\delta\varphi)\rangle = -0.16(5)$. Ideally these values would vanish for a perfectly random distribution. We attribute the residual deviations to a systematic error in our fit-

ting protocol, which is mainly caused by the non-uniform shape of the overall time-of-flight distribution. The assumption of initially uncorrelated BECs is further supported by additional experimental tests, where we have measured the probability distribution for $N = 9$ for different thicknesses of the potential barriers and did not observe any significant change when varying the width by $\sim \pm 20\,\%$.
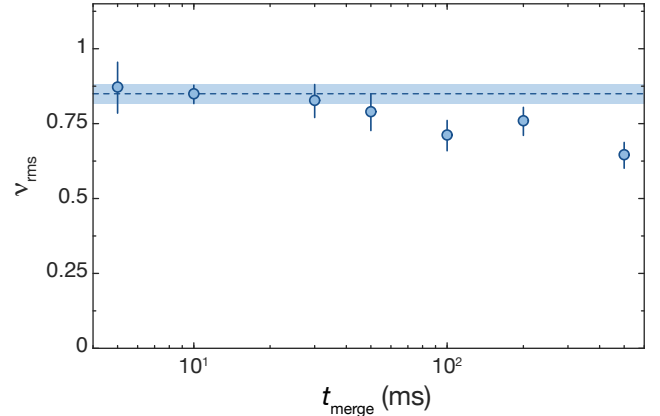

FIG. S3: Width of the distribution for $N = 9$ as a function of the merging time t_{merge}. Each data point was obtained from a set of 50-100 individual measurements. The data point at $10\,$ms corresponds to the merging time we used for the data presented in the main text and consists of $\mathcal{M} = 388$ measurements. The vertical error bars denote the statistical uncertainty due to a finite number of measurements $\mathcal{M}$ and the uncertainty in the determination of the winding numbers.

WIDTH OF THE DISTRIBUTION FOR DIFFERENT MERGING TIMES

For the measurements presented in the main text we merged the condensates within $10\,$ms. This time was chosen between two limiting regimes. If the condensates are merged too fast, we may create shock waves and high-energy excitations [S6, S7] as opposed to the quasi-adiabatic generation of supercurrents we want to probe in the experiment. On the other hand if the merging is performed too slowly, the formation of supercurrents with non-zero phase winding might be reduced due to an asynchronous closing of the individual barriers since the phase between neighboring condensates may homogenize before the merging is complete. Moreover, the lifetime of the supercurrents may be reduced in the presence of weak potential barriers around the ring when the supercurrents are formed during the merging [S4]. Experimentally we investigated these effects for $N = 9$ initial condensates. We found that varying the merging time by about one order of magnitude between $5\,$ms and $50\,$ms did not significantly influence our experimental results (Fig. S3).

When the barriers were removed abruptly instead we observed a significant increase in the width of the distribution $\nu_{\rm rms}$ and the interference pattern exhibited many phase defects.

LIFETIME OF SUPERCURRENTS

For the measurements reported in the main text we typically wait $0.5\,$s after merging the condensates. We have studied the lifetime of the supercurrents using the same experimental sequence and increasing the waiting time before detection. The results are displayed in Fig. S4. We observed no significant decay of the supercurrents for waiting times that are on the order of the atomic lifetime (inset Fig. S4). This timescale is large compared to timescale of a typical experimental sequence.
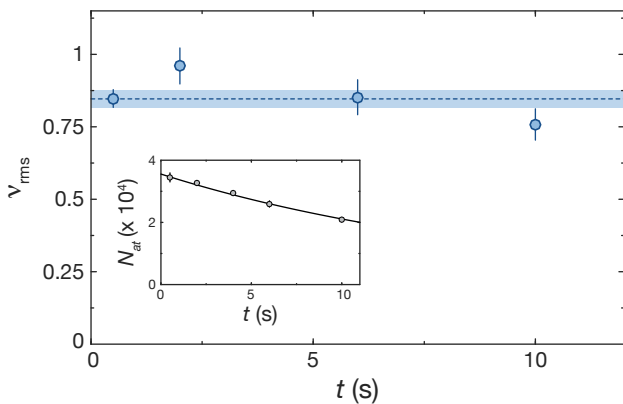

FIG. S4: Lifetime of supercurrents and atoms for $N = 9$ segments. The data points show the measured rms-width $\nu_{\rm rms}$ as a function of time t after merging the condensates. Each data point was evaluated from $\mathcal{M} > 100$ images. The data point at $t = 0.5\,$s corresponds to the typical experimental sequence with $\mathcal{M} = 388$ [Fig. 2(a) in the main text]. It is further highlighted by the dashed line, the shaded area represents its uncertainty. All error bars display the combined error of statistical uncertainties and uncertainties in the analysis of the interference patterns. The inset displays the corresponding atom numbers. For each data point we evaluated between 2 and 13 measurements and the vertical error bars depict the standard deviation. The solid line is the fit of an exponential function $f(t) = A\mathrm{e}^{-t/\tau}$ to our data, resulting in $\tau = 19(1)\,$s.

CENTER VALUES FOR THE RELAXATION MEASUREMENTS

In Fig. S5 we display the mean values $\bar{\nu}$ of the distributions corresponding to the data displayed in Fig. 3 of the main text, where we have studied the relaxation from N to $N/2$ condensates, when merging them in two successive steps. For $N = 6$ initial segments we observe

consistently larger asymmetries in the distributions and they seemed to be reproducible over the course of several days. In the case of $N = 12$ the observed asymmetries are consistent with statistical fluctuations.
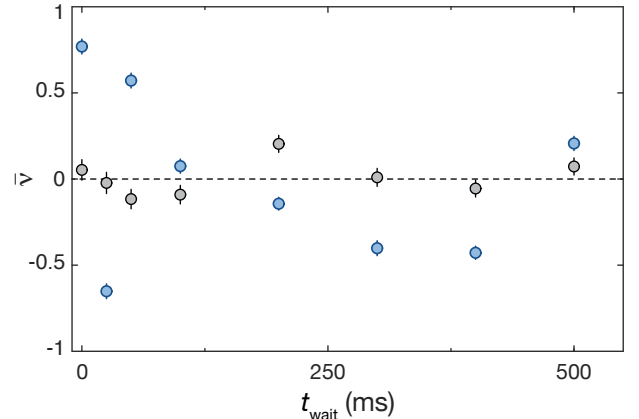

FIG. S5: Center values $\bar{\nu}$ of the distributions corresponding to the widths $\nu_{\rm rms}$ shown in Fig. 3 of the main text for $N = 12$ (black) and $N = 6$ (blue) respectively. Each data point consists of $\mathcal{M} > 200$ measurements. The vertical error bars depict the standard deviation obtained from statistical uncertainties and the experimental uncertainty in the determination of the winding numbers.

EXPERIMENTAL SEQUENCE AND DATA ANALYSIS FOR THE MERGING OF TWO CONDENSATES

The experimental sequence for the study of the dynamics of the defects was as follows: We loaded a rectangle of size $50 \times 30\,\mu$m with thermal atoms and dynamically reduced its width to $13\,\mu$m within $0.2\,$s. A separation of width $3\,\mu$m was abruptly introduced in the middle of the rectangle to create two lines of dimensions $50 \times 5\,\mu$m. One of the lines was further cut into two lines of length $23.5\,\mu$m. The other line serves as a phase reference for the detection. The system was then cooled down within $2\,$s to the same temperature as given in the main text. After an equilibration time of $1\,$s the separation between the two $23\,\mu$m-long lines was removed within $9.5\,$ms, following the same procedure as discussed in the previous sections. We then let the system relax for a variable time $t_{\rm wait}$ and subsequently detected the interference pattern by performing a 2D-TOF of $3\,$ms (as introduced in the section *Experimental sequence*) followed by a 3D-TOF of $3\,$ms during which we removed all confining potentials.

Phase defects in the interference pattern were analyzed in the following way: We chose a region-of-interest in the center of the cloud in the x-direction, which represents two periods of the fringes (Fig. S6a) and performed a sliding average of the image along y to smoothen the
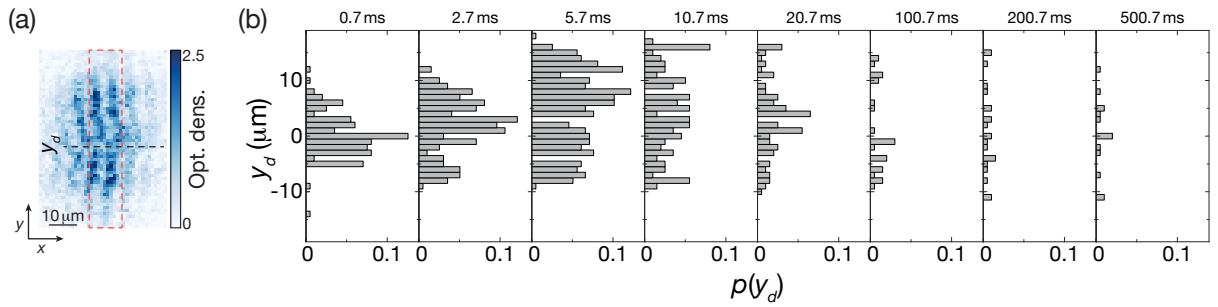
FIG. S6: (a) Interference pattern after an evolution time $t_{\text{wait}} = 0.7\,\text{ms}$ detected after a 2D-TOF of 3 ms plus a 3D-TOF of 3 ms. The red-dashed lines mark the region-of-interest for the data analysis. The phase dislocation at x_d his highlighted by a black dashed line. (b) Position distributions $p(y_d)$ of the phase dislocations for various evolution times t_{wait}. The histograms are normalized by the total number of images. For each time t_{wait} we have taken about 200 individual measurements. For this data the threshold for the analysis described in the text is $\varphi_c = 0.3\pi$.

profile. The wavevector of the fringes along x was determined via Fourier transform. For each position in the y-direction, the modulus of this Fourier coefficient gives us the visibility of the fringes and its phase is the local relative phase of the two lines at this position. The dislocations can be found at the positions where both the visibility drops and the phase jumps. More precisely we were looking for coincidences of minima of the visibility and maxima of the absolute value of the phase gradient along the y-direction. We removed an overall smooth gradient of the phase across the whole cloud to avoid any systematic bias between positive and negative phase jumps. We evaluated the data for different threshold values φ_c between neighboring pixels (this corresponds to an effective pixel size of $1.16\,\mu\text{m}$ in the atomic plane), where a phase dislocation is detected above this threshold. All phase dislocations below this value are discarded. This threshold is needed in order to avoid the detection of false dislocations. The extracted positions y_d of the detected phase dislocations are shown in the histograms (Fig. S6b), which are normalized by the total number of individual measurements.

In order to evaluate the total number of defects N_d (Fig. 4c in the main text) as a function of time we assume that phase jumps occur with an equal probability in the interval $(-\pi, \pi]$. The threshold value φ_c will artificially reduce the number of detected defects by a factor $(1 - \varphi_c/\pi)$. Therefore we use this as a correction factor and

rescale our data accordingly. This is certainly true for short times but it is not necessarily the case for long times because the relaxation dynamics most likely depend on the initial phase difference between the two condensates. Nonetheless it helps us to estimate the error we make in the data analysis due to the finite threshold value φ_c. In Fig. 4c of the main text we display the results for different threshold values between 0.16π and 0.43π.

———

[S1] J. L. Ville, T. Bienaimé, R. Saint-Jalm, L. Corman, M. Aidelsburger, L. Chomaz, K. Kleinlein, D. Perconte, S. Nascimbène, J. Dalibard, et al., Phys. Rev. A **95**, 013632 (2017).

[S2] S. Eckel, F. Jendrzejewski, A. Kumar, C. J. Lobb, and G. K. Campbell, Phys. Rev. X **4**, 031052 (2014).

[S3] L. Corman, L. Chomaz, T. Bienaimé, R. Desbuquois, C. Weitenberg, S. Nascimbène, J. Dalibard, and J. Beugnon, Phys. Rev. Lett. **113**, 135302 (2014).

[S4] A. Ramanathan, K. C. Wright, S. R. Muniz, M. Zelan, W. T. Hill III, C. J. Lobb, K. Helmerson, W. D. Phillips, and G. K. Campbell, Phys. Rev. Lett. **106**, 130401 (2011).

[S5] R. T. Bailey, Risk Analysis **17**, 375 (1997).

[S6] J. J. Chang, P. Engels, and M. A. Hoefer, Phys. Rev. Lett. **101**, 170404 (2008).

[S7] R. Meppelink, S. B. Koller, J. M. Vogels, P. van der Straten, E. D. van Ooijen, N. R. Heckenberg, H. Rubinsztein-Dunlop, S. A. Haine, and M. J. Davis, Phys. Rev. A **80**, 043606 (2009).